

Coupled mooring analysis for floating wave energy converters using CFD: Formulation and validation



Johannes Palm ^{a,*}, Claes Eskilsson ^a, Guilherme Moura Paredes ^b, Lars Bergdahl ^a

^a Department of Shipping and Marine Technology, Chalmers University of Technology, SE-412 96 Gothenburg, Sweden

^b Department of Civil Engineering, Faculty of Engineering, University of Porto, 4200-465 Porto, Portugal

ARTICLE INFO

Article history:

Received 1 October 2015

Revised 25 February 2016

Accepted 3 May 2016

Available online 10 May 2016

Keywords:

Wave energy

Point-absorbers

Navier–Stokes equations

Mooring dynamics

Coupled simulations

ABSTRACT

Floating wave energy converters (WECs) operating in the resonance region are strongly affected by non-linearities arising from the interaction between the waves, the WEC motion and the mooring restraints. To compute the restrained WEC motion thus requires a method which readily accounts for these effects. This paper presents a method for coupled mooring analysis using a two-phase Navier–Stokes (VOF–RANS) model and a high-order finite element model of mooring cables. The method is validated against experimental measurements of a cylindrical buoy in regular waves, slack-moored with three catenary mooring cables. There is overall a good agreement between experimental and computational results with respect to buoy motions and mooring forces. Most importantly, the coupled numerical model accurately recreates the strong wave height dependence of the response amplitude operators seen in the experiments.

© 2016 The Authors. Published by Elsevier Ltd. This is an open access article under the CC BY license (<http://creativecommons.org/licenses/by/4.0/>).

1. Introduction

Accurate tools for design and numerical modelling of floating wave energy converters (WECs) are essential to the development of the wave power industry. There is a large variety of concepts for wave energy extraction, each with their own set of challenges, and they all struggle towards cost reduction for commercial viability [1]. Design rules and modelling tools from the offshore industry are used when applicable, but wave power companies rely heavily on experimental tests in model scale, as well as on large scale sea trials. Such tests are costly and not well-suited for parametric studies of the design variables. If the accuracy and reliability of computational models at all stages of the design cycle are increased, the desired outcome of tests and trials is more likely to be achieved. In this way an economically favourable development path can be followed, where the device performance is optimised in an early stage [2].

A special class of floating WECs is the point absorbers. These devices are generally small in relation to the wave length and are typically subjected to large amplitude motions close to resonance. Because of their limited size, they are also significantly influenced by mooring restraints [3]. Some concepts have a small or non-existing freeboard [1], which increases the probability of green-water on the floating body. The state-of-the-art design tool for hydrodynamic modelling of WECs is linear radiation-diffraction models with additional correction terms for non-linear effects. Including the non-linear Froude–Krylov force as in [4], and/or the parametrised viscous drag forces as in [5,6], shows promising results for extending the range of validity of these fast codes. However, the correction terms are based on a parametrization of the non-linearities of the system, and therefore there are cases where a more complete and general model approach is needed.

* Corresponding author.

E-mail address: johannes.palm@chalmers.se (J. Palm).

An advanced approach to model the highly non-linear system of floating point absorbers is to use incompressible two-phase Reynolds averaged Navier–Stokes (VOF–RANS) simulations. This family of computational fluid dynamics (CFD) methods inherently includes non-linear waves, viscous flow characteristics, green-water and large amplitude motion effects, although the computational cost is orders of magnitude higher than for linear radiation-diffraction methods. VOF–RANS is nowadays engineering standard for ship hydrodynamics [7], extending into coastal applications [8–10]. For offshore semi-submersibles, CFD simulations are becoming an integrated part of the design cycle [11]. The CFD simulations are then used to limit the need of experimental tests. Experimental data is used to validate the CFD methodology, but later design iterations can be based on simulations using faster radiation-diffraction models, which in turn are validated by CFD simulations of the updated designs.

Several studies have used CFD to model floating WECs in one or two degrees of freedom (DoF), while comparing with results from faster methods of lower fidelity [5,12,13]. The general conclusion is that non-linear effects such as viscous drag and non-linear wave loading can have a large impact on power production estimates, and that the numerical models for power production should take this into account. CFD studies of moored WECs tend to use a simplified linear spring equivalence to model the mooring dynamics [14,15]. Fully coupled CFD-mooring analysis was presented in [16] for the OWEL device in surge, heave and pitch, using a ANSYS-CFX to Orcaflex coupling. They obtain good results, but the coupling procedure is not described in detail. A six DoF moored WEC was modelled in [17], although without a validation of the coupled method. As was pointed out by Wolgamot and Fitzgerald [18], there is still a need of validated, generic CFD studies dealing with the non-linearities of floating WECs.

The aim of this paper is to present a method for fully coupled CFD-mooring analysis of moored floating objects, including a validation study. We have implemented a coupling between VOF–RANS simulations using the OpenFOAM® [19] framework, and an in-house mooring solver. OpenFOAM has been used in several studies of wave energy applications, see [20] and references therein. The mooring software, MooDy, has been shown to compare well with experimental data [21–23]. The coupled model adds dynamic and non-linear mooring interaction between the cables and the floating body to the capabilities of the native VOF–RANS method, and thereby presents a solid framework for simulating highly non-linear behaviour of WECs. There is also support for including power take off (PTO) and its influence on the motion response of the WEC, however the computational examples are in this study for a moored buoy without PTO. The coupled method is validated for a set of regular waves from small scale experiments of a cylindrical buoy, moored with three symmetrically placed catenary chains, taken from [24]. Computed results of surge, heave, pitch and mooring force are compared with experimental data.

The paper is organised as follows. Section 2 presents the Navier–Stokes equations and the methodology of the fluid domain solution in the open-source framework OpenFOAM. Section 3 describes the governing equations of mooring cable dynamics and the in-house mooring solver MooDy. The coupling between the fluid and the mooring solvers are presented in Section 4. In Sections 5 and 6 we present the experimental and computational setups respectively. The computational results are presented in Section 7 and include mesh independence checks, decay tests, general flow characteristics, and motion and force time histories of the body and moorings in regular waves. The paper ends with the concluding remarks in Section 8.

2. Fluid domain

2.1. Free-surface Navier–Stokes simulations

The governing incompressible Reynolds Averaged Navier Stokes (RANS) equations of the flow can be written as

$$\nabla \cdot \mathbf{u} = 0, \quad (1)$$

$$\frac{\partial}{\partial t}(\rho \mathbf{u}) + \nabla \cdot (\rho(\mathbf{u} - \mathbf{u}_g)\mathbf{u}) = -\nabla p + \nabla \cdot \mathbf{S} + \rho \mathbf{f}_b. \quad (2)$$

Here \mathbf{u} is the fluid velocity, \mathbf{u}_g is the grid velocity, p is the pressure, and ρ is the density of the fluid. The viscous stress tensor

$$\mathbf{S} = 2\mu \mathbf{D}, \quad (3)$$

is a function of the dynamic viscosity μ and the rate-of-strain tension \mathbf{D} . The body force \mathbf{f}_b includes buoyancy and surface tension effects. The free surface is captured using the volume of fluid (VoF) method, where the two-phase problem is treated as a single fluid with an additional volume-fraction parameter $\alpha \in [0, 1]$, subject to the transport equation

$$\frac{\partial \alpha}{\partial t} + \nabla \cdot (\alpha(\mathbf{u} - \mathbf{u}_g)) = 0. \quad (4)$$

In each cell, the fluid properties are then computed as a mixture between air ($\alpha = 0$) and water ($\alpha = 1$):

$$\rho = \alpha \rho_w + (1 - \alpha) \rho_a, \quad (5)$$

$$\mu = \alpha \mu_w + (1 - \alpha) \mu_a, \quad (6)$$

where index w and a indicate water and air respectively.

Eqs. (1), (2) and (4) are solved using the interDyMFoam solver provided in OpenFOAM [19], version 2.3. OpenFOAM is a cell-centred finite volume framework for computational fluid dynamics supporting unstructured polyhedral meshes [25]. interDyMFoam is a segregated, iterative solver using the PIMPLE algorithm, with support for dynamic mesh motion. A large number of turbulence models are supported for RANS simulations, but there is no consensus about which to use for wave propagation problems. The flow is sometimes modelled as laminar or inviscid, see e.g. [26,8,13]. Yu and Li [12,15] used the $k-\omega$ SST model, and Ruju et al. [27] used the $k-\epsilon$ model with closure according to [28]. We model the viscous terms as in [9], using the RNG $k\epsilon$ turbulence model.

We employ the waves2Foam package [26] to make suitable boundary conditions, using separate relaxation zones for wave generation and for wave absorption upstream and downstream of the body. Inside the relaxation zones, the computed solution of velocity and volume fraction (u_c, α_c) are relaxed by blending with an analytical target solution (u_t, α_t):

$$u_c = u_t w(\mathbf{x}) + u_t (1 - w(\mathbf{x})), \quad (7)$$

$$\alpha_c = \alpha_t w(\mathbf{x}) + \alpha_t (1 - w(\mathbf{x})). \quad (8)$$

Here the spatially varying weighting function $w(\mathbf{x}) \in [0, 1]$ is 0 at the outer (domain) boundary and 1 at the internal boundary of the relaxation zone.

2.2. Rigid body dynamics

The motions of the cylinder are computed by the native rigid body solver of OpenFOAM that uses a nested explicit leap-frog time step within each PIMPLE loop. Resulting forces and moments are collected from integration of the pressure force, $p\hat{\mathbf{n}}$, and shear force vector τ over the body surface S as

$$\mathbf{F} = \iint_S (p\hat{\mathbf{n}} + \tau) dS + \mathbf{F}_M + \mathbf{F}_{PTO}, \quad (9)$$

$$\mathbf{M} = \iint_S (\mathbf{r}_{CS} \times (p\hat{\mathbf{n}} + \tau)) dS + \mathbf{r}_{CM} \times \mathbf{F}_M + \mathbf{M}_{PTO}. \quad (10)$$

Here \mathbf{F}_M is the mooring force from MooDy – see Section 3 – and position vectors \mathbf{r}_{CM} and \mathbf{r}_{CS} denote the vector from the centre of mass to the mooring attachment point and the centre of each surface panel respectively. The pair \mathbf{F}_{PTO} and \mathbf{M}_{PTO} represents the additional force and moment from an external power take off (PTO). In this study, no PTO was modelled.

2.3. Mesh motion

The computational grid deforms with the motion of the body. Deformation of each grid point is scaled from the full rigid body displacement to no deformation based on the distance to the cylinder surface, $r \in [r_i, r_o]$ using spherical linear interpolation. r_i and r_o define the inner and outer distance of the scaling respectively. Thus, points at $r \leq r_i$ are locked to the rigid body to avoid deforming very fine cells, and points at $r \geq r_o$ are part of a static mesh. Typically r_i is in the order of the boundary layer thickness, and r_o is limited by the minimum distance to any domain boundary.

3. Mooring cable dynamics

This study uses the in-house software MooDy [21] for computing the mooring cable dynamics. MooDy is a high-order finite element model. The equation of motion of a perfectly flexible cable can be expressed as a vector-valued wave equation with non-linear coupling via the axial tension force \mathbf{T} , and the axial strain ϵ . The cable position $\mathbf{r} = (r_x, r_y, r_z)$ expressed along the curvilinear abscissa s of the unstretched cable domain is governed by

$$\frac{\partial^2 \mathbf{r}}{\partial t^2} = \frac{1}{\gamma_0} \frac{\partial \mathbf{T}}{\partial s} + \frac{\mathbf{f}}{\gamma_0}, \quad (11)$$

$$\mathbf{T} = T(\epsilon, \dot{\epsilon}) \frac{\mathbf{q}}{1 + \epsilon}, \quad (12)$$

$$\mathbf{q} = \frac{\partial \mathbf{r}}{\partial s}, \quad (13)$$

$$\epsilon = |\mathbf{q}| - 1, \quad (14)$$

where γ_0 is the cable mass per meter. All external forces are represented by \mathbf{f} and an auxiliary variable \mathbf{q} is introduced to achieve only first order expressions in space. $T(\epsilon, \dot{\epsilon})$ is the tension force magnitude, which contains the constitutive relation of the cable material as a function of the strain and strain rate of the cable. In the case of a linear elastic cable material with axial stiffness EA_0 , the tension appears as

$$T(\epsilon) = EA_0\epsilon. \quad (15)$$

The external forces

$$\mathbf{f} = \mathbf{f}_a + \mathbf{f}_b + \mathbf{f}_c + \mathbf{f}_d, \quad (16)$$

acting on each cable segment are separated into:

\mathbf{f}_a : Added mass force and Froude–Krylov force,

\mathbf{f}_b : Buoyancy and gravity force,

\mathbf{f}_c : Contact force,

\mathbf{f}_d : Drag force.

Let the unit tangential vector \mathbf{t} be written as

$$\mathbf{t} = \frac{\partial \mathbf{r}}{\partial s} / \left| \frac{\partial \mathbf{r}}{\partial s} \right| = \frac{\partial \mathbf{r}}{\partial s} / (1 + \epsilon), \quad (17)$$

and the index notation for tangential and bi-normal projection of any vector quantity \mathbf{x} respectively be

$$\mathbf{x}_t = (\mathbf{x} \cdot \mathbf{t})\mathbf{t}, \quad (18)$$

$$\mathbf{x}_n = \mathbf{x} - \mathbf{x}_t. \quad (19)$$

In terms of these notations, added mass, buoyancy and drag forces are expressed as

$$\mathbf{f}_a = \rho_f A_0 (C_{Mt} \mathbf{a}_{r,t} + C_{Mn} \mathbf{a}_{r,n} + \mathbf{a}_f), \quad (20)$$

$$\mathbf{f}_b = \gamma_0 \left(\frac{\rho_c - \rho_f}{\rho_c} \right) \mathbf{g} = \gamma_e \mathbf{g}, \quad (21)$$

$$\mathbf{f}_d = \frac{1}{2} \rho_f d \sqrt{1 + \epsilon} (C_{Dt} |\mathbf{v}_{r,t}| \mathbf{v}_{r,t} + C_{Dn} |\mathbf{v}_{r,n}| \mathbf{v}_{r,n}), \quad (22)$$

where ρ_f is the density of the surrounding fluid (being air density above the water surface, and water density below it), d is the cable diameter, A_0 is the unstretched cross-sectional area of the cable, and coefficients (C_{Mt}, C_{Mn}) and (C_{Dt}, C_{Dn}) denote added mass and drag coefficients in the tangential (index t) and normal (index n) direction respectively. Further, $\mathbf{g} = [0, 0, -g]$ is the earth acceleration ($g = 9.81 \text{ ms}^{-2}$) and vectors \mathbf{a}_r and \mathbf{v}_r are relative accelerations and velocities of the cable through the water, i.e.

$$\mathbf{v}_r = \mathbf{v}_f - \mathbf{v}, \quad (23)$$

$$\mathbf{a}_r = \mathbf{a}_f - \mathbf{a}, \quad (24)$$

where again, index f denotes the surrounding fluid (air or water), and \mathbf{v} and \mathbf{a} are the velocity and acceleration vectors of the cable.

The contact force \mathbf{f}_c is the force acting on the cable from the sea bed. In the normal direction this is modelled as in [29], with a bi-linear spring and damper formulation:

$$f_{c,z} = \begin{cases} Kd(r_z - z_g) - 2\xi\sqrt{\gamma_0 Kd} \max(v_z, 0) & \text{if } r_z \leq z_g \\ 0 & \text{otherwise,} \end{cases} \quad (25)$$

where K is the Winkler module (Pa/m) and $\xi \geq 0$ is the ratio of critical vertical damping. Along the tangential plane, there is a viscous friction force as in [30], proportional to the dynamic friction coefficient μ as

$$\mathbf{v}_{xy} = \frac{(v_x, v_y)}{\max(v_c, |(v_x, v_y)|)} \quad (26)$$

$$\mathbf{f}_{c,xy} = -\gamma_e g \mu \sin\left(\mathbf{v}_{xy} \frac{\pi}{2}\right), \quad (27)$$

where v_c is the speed of fully developed friction force magnitude.

MooDy is spatially discretised with the local discontinuous Galerkin (LDG) method with Legendre basis functions of arbitrary order p . The LDG formulation was first proposed in [31]. The numerical implementation of MooDy is described in further detail in [32,21]. One of the most prominent features of high-order methods is the exponential convergence for smooth solutions, such as the hanging catenary. Thus engineering accuracy is achieved using only a few elements of high order. High-order methods are however known to be prone to Gibbs-type oscillations in cases when the solution is non-smooth, such as at the touch-down point of the catenary chain.

We use explicit time stepping with second order accurate Leap-Frog scheme to advance in time. The range of numerically stable time step sizes in an explicit scheme is then restricted by the mesh size h , the mesh order p and the speed of sound in the cable ($c = \sqrt{EA_0/\gamma_0}$). As the cable stiffness is high, the time step of MooDy is in general much smaller than that of the fluid solver.

4. Coupling procedure

4.1. Algorithm

The mooring attachment point positions on the buoy are used as Dirichlet boundary conditions for the mooring solver. Through the coupling the corresponding mooring force from each cable is then returned to the fluid domain to solve for the coupled rigid body motion. The fluid solver has a typical time step in the range of $\Delta t^{\text{OF}} \in [10^{-2}, 10^{-4}]$ s in this model scale simulation, and the mooring solver time step is $\Delta t^{\text{M}} \sim 10^{-5}$ s. Because of the different time scales, the boundary values need to be interpolated in time using a sub-stepping routine.

The interpolation used is best described as a lagging quadratic interpolation. Letting t_k^{OF} be the fluid solver time at time step k , the mooring solver is lagging a fraction ϕ of the latest time step of the fluid solver and is thus slightly behind:

$$t_k^{\text{M}} = (1 - \phi)t_k^{\text{OF}} + \phi t_{k-1}^{\text{OF}}, \quad (28)$$

where t_k^{M} is the k th time of the mooring code. For each new fluid time step t_k^{OF} , the mooring position P_k is used to compute the interpolated mooring cable boundary conditions. Position $r_k(\tau)$ and velocity $v_k(\tau)$ of the cable end point are expressed in terms of the local time of the interpolated interval $\tau \in (0, t_k^{\text{M}} - t_{k-1}^{\text{M}}]$, using constant acceleration. Thus

$$r_k(\tau) = r(0) + (v(0) + 0.5a_k\tau)\tau, \quad (29)$$

$$v_k(\tau) = v(0) + a_k\tau, \quad (30)$$

$$a_k = \frac{1}{0.5\Delta_k^2}(P_k - r_k(0) - v_k(0)\Delta_k), \quad (31)$$

where $\Delta_k = t_k^{\text{OF}} - t_{k-1}^{\text{M}}$ is the time interval of constant acceleration. The mooring force F_k is then returned as the force at t_k^{M} , and the fluid solver continues to solve for the restrained motion of the body.

Using a lagging scheme for the coupling ensures smooth and continuous velocities and positions at the time-step boundaries. If $\phi = 0$, the method is in phase, but velocity is limited to a first order approximation. It should be noted that although the lagging interpolation effectively avoids spurious oscillations of the interpolation, it also dampens high-frequency motions of the end-point. The boundary motion is smoothed over an additional ϕ fraction of the time step, and therefore a sufficient sampling frequency of the main solver is needed for the algorithm to converge. In this application, the motion of the mooring points follow the rigid body motion of the buoy, which is smooth and well-sampled in the fluid flow solver. Thus, the boundary motion is well described by the sub-stepping interpolation scheme.

4.2. Implementation

The coupling algorithm described above is implemented inside the automated program interface (API) of MooDy, making it easier to couple to different solvers for the hydrodynamics. The six DoF motion solver in OpenFOAM is the primary solver, and MooDy acts as a secondary solver called from inside the class hierarchy of OpenFOAM. The API is called from a special purpose restraint class of the six DoF solver.

5. Case description

5.1. Physical model

A generic buoy was experimentally tested in a wave tank with a water depth of 0.9 m in [24]. The buoy is a vertically truncated cylinder of mass $M = 35.85$ kg, diameter $D = 0.515$ m, and moment of inertia around the centre of gravity $I_{xx} = 0.9$ kg m². The centre of gravity is placed 0.0758 m above the bottom of the buoy along the symmetry z-axis. These values are the ones used in setting up the numerical model and are modified from [24] to include the extra mass (0.35 kg) and inertia (0.03 kg m²) from the styrofoam lid and the metal supports of the moorings that were attached to the buoy.

The three mooring cables were catenary chains placed symmetrically 120° apart, with one cable attached on the leeward side directed along the propagation direction of the long-crested waves; see Fig. 1. Mooring attachment points were at the water line, 0.015 m out from the buoy side. The cable properties used in the numerical model were compiled from measurable quantities given in [24], and numerical coefficients from simulations of a similar chain in [23]. The chain properties are presented in Table 1.

6. Numerical modelling

6.1. Computational settings

The computational fluid domain contains 8.3 million cells in a rectangular box: $x \in [-6, 9]$ m, $y \in [-2.5, 2.5]$ m, $z \in [-0.9, 0.9]$ m, with the buoys centre of gravity initially located at $(x, y, z) = (0, 0, -0.096)$ m. The initial draft of the buoy

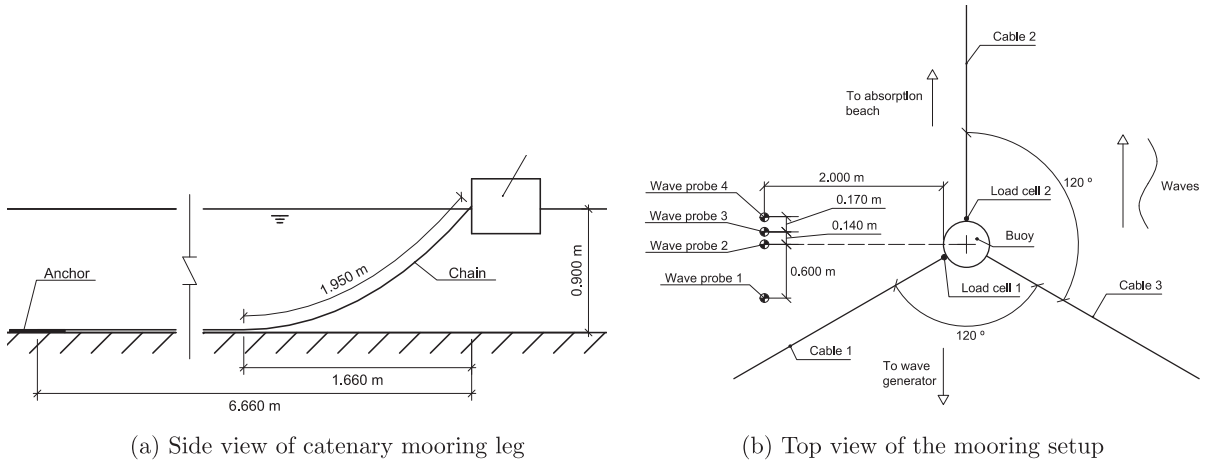


Fig. 1. Geometric description of the experimental setup and the mooring cable configuration.

Table 1

Properties of the chain and environmental parameters used in the mooring simulations. Values compiled from [24,23].

Symbol	Quantity	Value	Unit
γ_0	Mass	0.1447 ± 0.0001	kg/m
$\gamma_e g$	Submerged weight	1.243 ± 0.006	N/m
d	Diameter	4.786×10^{-3}	m
C_{Mt}	Tangential added mass coefficient	0	–
C_{Mn}	Normal added mass coefficient	3.8	–
C_{Dt}	Tangential drag coefficient	0.5	–
C_{Dn}	Normal drag coefficient	2.5	–
K	Ground stiffness	300	MPa/m
C	Ground damping coefficient	1	–
μ	Ground friction coefficient	0.3	–
v_c	Velocity of dynamic friction, ground	0.01	m/s

was set to 0.172 m, being the equilibrium of the free floating buoy. The static offset of the moorings was then handled by mesh deformation. Wave generation and absorption was made through relaxation zones of length 3 m at the inlet and 6 m from the outlet, comparing to 1–2 wavelengths for generation and 2–4 wavelengths for absorption (see Table 2). Thus the buoy was surrounded by 3 m of free computational domain on both sides of its initial position. To support wave propagation without excessive wave damping, there is a band of refined cells around the free surface, see Fig. 2. The outer regions are supported only with a coarse grid in the span-wise direction (y), as no transverse flow except that created by the presence of the buoy is expected for long-crested waves. In the near-field area, the mesh is refined to capture the radiation-diffraction forces on the body and the turbulent fluctuations near the boundary layer accurately. Towards the outlet, the mesh is also coarser in the x and z directions to decrease the computational cost.

Viscous effects near walls are characterised by the non-dimensional wall distance $y^+ = \frac{u^*y}{\nu}$, where u^* is the friction velocity, y is the distance to the wall, and ν is the kinematic viscosity of the fluid. In this study we employ wall functions to approximate the viscous quantities in the boundary layer surrounding the cylinder. For this to be properly modelled, we require the y^+ values of the simulations to be in the order of $y^+ \in [25 – 100]$.

There is a wide variety of settings and choices of numerical schemes in OpenFOAM. The convection terms were in this study modelled using a centred total variation diminishing (TVD) scheme (limitedCubic) for the momentum and a second order TVD limiter (SuperBee) for the volume fraction. Gradient and diffusion operators were solved using a second order central difference scheme (linear). Surface compression with a factor $c_\alpha = 0.5$ was used in the simulations, and the Euler backward scheme with adaptive time step size based on a maximum Courant number of 0.5 was used for time integration.

The three mooring cables were each simulated with 10 elements of order 6, ($N = 10, P = 6$) in MooDy. An explicit leap-frog time stepping scheme with a fixed time step of 1×10^{-5} s was used for time integration of the mooring solution, with a time lag fraction of 0.5 in relation to the CFD domain time step (see Section 4). Please note that no filters have been applied in the mooring solver.

6.2. Load cases

Computational results are presented for the buoy decay response in surge, heave and pitch, and for a subset of the long-crested regular waves tested with the physical model. Based on the experimentally determined resonance periods of heave

Table 2

Description of the six long-crested regular waves used in the simulations, characterised by period time T , wave height H , wave length λ , wave steepness H/λ , Reynolds number (Re) and Keulegan–Carpenter number (KC).

Label	T (s)	H (cm)	λ (m)	H/λ (-)	Re ($\times 10^5$)	KC (-)
T10H4	1.0	4	1.57	0.026	0.647	0.244
T12H4	1.2	4	2.23	0.018	0.539	0.244
T14H4	1.4	4	2.94	0.014	0.462	0.244
T10H8	1.0	8	1.59	0.050	1.294	0.488
T12H8	1.2	8	2.24	0.036	1.079	0.488
T14H8	1.4	8	2.94	0.027	0.925	0.488

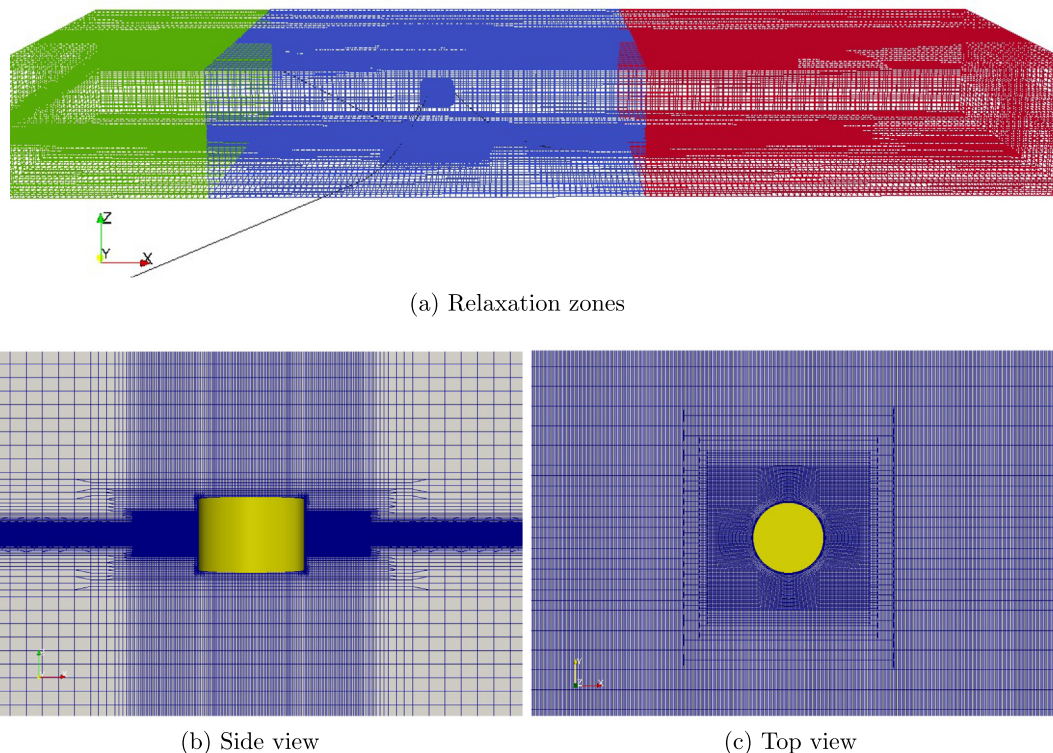


Fig. 2. Outline of the undeformed computational mesh surrounding the floating body. In (a) green indicates wave generation, blue indicates free domain and red indicates wave absorption.

and pitch (1.13 s and 1.16 s), three regular wave periods were selected to represent shorter waves ($T = 1.0$ s), waves in the resonance region ($T = 1.2$ s), and longer waves ($T = 1.4$ s). Two wave heights ($H = 4$ cm and $H = 8$ cm) were tested for each period to investigate if the wave height dependence on the RAOs seen in the experiments is correctly captured by the numerical model. Table 2 shows the characteristics of the six regular wave cases together with the labelling of each used in the results Section 7. The steepness of the waves ranges from 1.4 to 5% and are generated as Stokes 5th order waves. It is worth noting that only two cases are expected to be in accordance with linear theory, using the engineering rule-of-thumb of maximum 2% steepness.

The Keulegan–Carpenter (KC) numbers in Table 2 are calculated approximately as $KC = u_0 T / D = \pi H / D$, with D being the buoy diameter and $u_0 = \pi H / T$ being the particle speed at the surface of the corresponding deep water linear wave [33]. The KC numbers indicate that drag forces should be limited in relation to inertia forces for these cases. The Reynolds numbers in Table 2 are computed from $Re = u_0 D / v$, where v is the kinematic viscosity of water, and u_0 is used as the free stream velocity. The range of Re numbers indicates that the flow characteristics should be similar between the simulations [34]. KC and Re are here included as indications of the expected flow characteristics of the tests. As the buoy moves with considerable amplitude in response to the waves, it is difficult to establish a clear correlation between these numbers and the numerical results.

6.3. Boundary conditions

The wave generation and absorption is made with relaxation zones (see Fig. 2a) with different target values specified at the inlet and outlet of the domain. At the inlet the target volume fraction α and the target velocity are taken from 5th order Stokes theory, and at the outlet they are set to model still water conditions. Relaxation weights using a free polynomial of order 10 were used to blend the analytic and computational waves. At the domain boundary the volume fraction and the water velocity thus match the analytic target wave, but the air phase velocity is there uniformly set to zero.

Boundary conditions for the turbulent quantities k and ϵ at the inlet are related to the celerity of the incoming wave, as proposed by [35]. It is important for stability reasons to have the correct order of magnitude of incoming turbulent quantities, but the results are not sensitive to smaller variations [35]. Therefore the same values were used for all waves in this study, based on the celerity of $T = 1.2$ s, $H = 4$ cm wave (T12H4).

6.4. Model approximations

There are always differences between the implementation of physical and numerical models. In this small model scale, expected uncertainties in measured data can have a visible impact on the results. For reasons of implementation some known approximations are made in the setup of the numerical model.

In the CFD simulations the buoy is perfectly truncated, but the experimental buoy was not perfectly so. The bottom corner was slightly rounded and bulged, and so was smoother than the right angle of the numerical model. The physical model also had protruding attachments for the moorings at the water level, thus changing the local flow pattern ever so slightly.

In the experiments, the fair-lead of the cable contained the load cell with connections (total of 4.6 cm). The mooring cable was modelled with homogeneous properties along its entire length in the simulations. This, in combination with a high sensitivity to variations of the cable length at such a small scale, rendered a 0.4 N offset of static tension between the two models. Please, also note that there is an inherent 0.2 N uncertainty in the experimental tension force readings [24].

Implementing a fluid coupling from the CFD domain to MooDy is still ongoing work. Therefore, the particle velocities and accelerations of the flow simulations are not affecting the added mass and drag forces acting on the cable. These forces are instead computed as if the cable is moving in still water conditions. Consequently the occasional cable emergence out of the water was not taken into account and the cable was simulated as submerged at all times during the simulations.

7. Results

7.1. Mesh resolution

A mesh sensitivity analysis was made by running the T12H4 regular wave case with four different meshes of increasing size, with the main mesh being the most refined. The T12H4 case was chosen because it is closest to resonance – giving the largest motions per wave height – and because of its lower wave amplitude, meaning that we have a smaller number of cells per wave height than in the $H = 8$ cm cases.

The mesh characteristics are shown in Table 3 together with the resulting wave amplitude and RAO of the motion relative to the results in the most resolved mesh (m3). Clearly the results are converging as the resolution increases, but a remarkably good result is obtained also for the meshes of lower resolution. We expect the discretization errors to increase as we go to shorter waves (to the $T = 1.0$ s case), and therefore the most resolved mesh (m3) was used to produce all other results presented in this paper. The excellent results with low resolution indicate that we use a sufficient mesh resolution and that we maintain a good resolution also for the more demanding wave cases.

The maximum y^+ values are listed in Table 4 for the different regular wave cases. All maximum values are within the range 33.4–84.9 (< 100), which also underlines that the resolution of the m3 mesh was indeed needed for the viscous boundary layer to be properly resolved.

7.2. Decay tests

The free decay of the buoy when released from a given excitation in surge, heave and pitch is used to establish the agreement between the physical and the experimental model setup, without the complexity of the incoming waves. Results from both the moored buoy (indexed Moor) and from the free case without moorings attached (indexed Free) are analysed in all three modes of motion.

Time series of the comparison between experimental and numerical results are presented in Fig. 3, and in Table 5 are shown the natural frequencies of the system. Experimental and numerical results compare well in the surge and the heave response, with numerical periods within 2% of the experimental results. Especially note that the surge decay in Fig. 3a is solely governed by the coupled effect of the mooring system. The surge period in Table 5 matches very well (1.5%), which validates that the dynamic mooring restraint is correctly modelled by the numerical method. The numerically predicted pitch response is however noticeably faster and more damped than the corresponding experiments, see Figs. 3c and e.

Table 3

Mesh characteristics and convergence indicators for the different meshes used in the mesh independence study. N is the total number of cells, Δx , and Δz are the largest cell sizes in the direction of wave propagation (x) and in the vertical (z) direction respectively. Δr is the cell size in the normal direction in the boundary layer around the cylinder. e represents the quota of wave amplitude or motion RAO between the results of the mesh and the mesh with maximum resolution (m^3).

Quantity	$m0$	$m1$	$m2$	$m3$
$N (1 \times 10^6)$	2.01	4.55	6.83	8.30
Δx (m)	0.0197	0.0142	0.0111	0.0098
Δz (m)	0.0018	0.0013	0.0011	0.0011
Δr (m)	0.0024	0.0016	0.0014	0.0012
$e^{\zeta} (-)$	0.932	0.975	0.992	1.000
$e_{RAO}^s (-)$	1.045	1.031	1.028	1.000
$e_{RAO}^h (-)$	1.053	1.019	1.008	1.000
$e_{RAO}^p (-)$	1.042	1.015	1.009	1.000

Table 4

Maximum y^+ values on the cylinder surface for all regular wave cases. Results are for the most resolved mesh ($m3$ in [Table 3](#)).

Wave height	$T = 1.0$ s	$T = 1.2$ s	$T = 1.4$ s
$H = 4$ cm	68.7	59.4	33.4
$H = 8$ cm	84.9	70.9	51.0

The pitch response is closely linked to the position of the centre of gravity relative to the water line, and the moment of inertia of the buoy. Therefore, acceptable measurement errors of physical quantities can result in noticeable differences in pitch for models of this small scale. To illustrate this point, results from a simple sensitivity analysis of the buoy properties centre of gravity and moment of inertia for the free pitch decay are shown in [Fig. 4](#). The centre of gravity was here moved 3 mm to 0.0788 m, and the moment of inertia was increased by 0.05–0.95 kgm². These changes were based on experimental uncertainties of buoy properties moment of inertia, centre of gravity and draft, reported in [\[24\]](#). As is seen in [Fig. 4](#), the altered model behaves much closer to the physical model in terms of natural period(^(CFD) $T_p = 1.163$ s). This shows that the present CFD model is quite sensitive to uncertainties in input data.

In general, the response from the CFD model is more damped than the experimental response, especially in pitch. There are a number of possible explanations for this, mostly related to viscous effects. The sharp corners of the numerical cylinder are expected to yield higher drag forces than the smoother physical model. In addition, the turbulence model and the use of wall functions might over-estimate the turbulent viscosity surrounding the body. Radiation damping of pitch is much

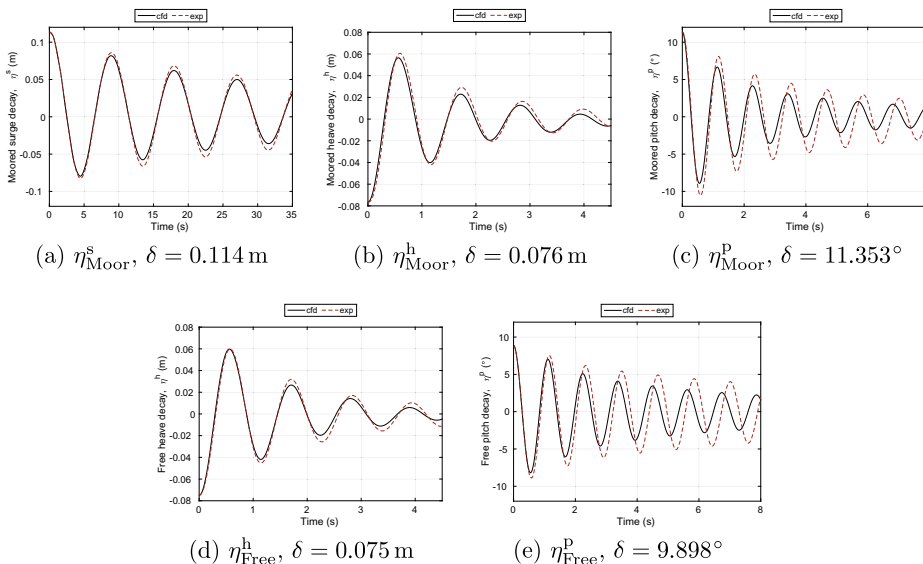


Fig. 3. Time series of the decay tests comparing numerical and experimental results. δ corresponds to initial offset from equilibrium in m for surge and heave, and in degrees ($^\circ$) for pitch. Index s, h, and p are used to label the surge, heave and pitch mode of motion respectively.

Table 5

Natural periods T of the buoy in surge, heave and pitch as determined by the decay tests. Experimental results and numerical values are shown for both free and moored decay. Index s, h, and p are used to label the surge, heave and pitch mode of motion respectively. Numerical results are based on averaging over the first N periods, where $N_s = 3$, $N_h = 4$, $N_p = 7$.

Quantity	EXP_{Free}	EXP_{Moor}	CFD_{Free}	CFD_{Moor}
T_s (s)	—	9.137	—	9.007
T_h (s)	1.112	1.130	1.100	1.109
T_p (s)	1.170	1.163	1.123	1.136

smaller than in heave for this type of body, and it is therefore expected that the viscous damping forces have a larger relative impact on the total damping in pitch than in heave.

7.3. Regular waves

Numerical simulations of the body motion in regular waves are here compared with measured values from six experiments. The wave parameters of the different tests are described in Table 2 and the comparison between computation and experiments is made with respect to (see Fig. 1b for geometry overview):

- ζ : surface elevation at the location of wave probe 2,
- $\bar{\eta}^s$: mean surge drift in the wave direction (x),
- η^s : surge response of the body's centre of floatation,
- η^h : heave response of the body's centre of floatation,
- η^p : pitch response of the body's centre of floatation,
- τ_1 : tension force magnitude at the fair-lead in cable 1,
- τ_2 : tension force magnitude at the fair-lead in cable 2.

Results are presented as time series, and in the case of the body responses η^s , η^h and η^p , also as response amplitude operators (RAOs). Further the numerical results (CFD) are analysed with respect to general flow characteristics, including vortical structures around the body.

7.3.1. General flow characteristics

A snapshot of the moored body moving in the T12H8 case is seen in Fig. 5. We see the radiation-diffraction pattern overlay on the pressure field. The influence is relatively small, as is to be expected from load cases with such a small KC number.

The vorticity magnitude is visualised in Fig. 6 showing results from the different $H = 8$ cm waves. Coherent turbulent structures are triggered mainly by the heave and pitch modes of motion. The four snapshots – taken 0.2 s apart – show the vorticity formation in the downstroke of the heave motion. A part of the vortical structures live on to be sucked in under the buoy in the upstroke of the motion. We also note the absence of a wake, and the turbulent effects remain highly local around the body. It is clear from that the vortical structures are similar for the different wave periods, which is as expected from the relatively narrow range of the Reynolds numbers (see Table 2). We also note that turbulent effects are smallest in the longer waves (T14H8) and that we get more coherent and long-lived vorticity tubes in the shorter waves.

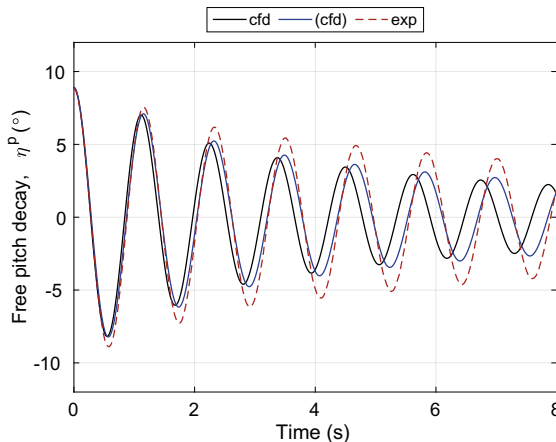


Fig. 4. Sensitivity of input parameters for free pitch decay. The cfd and exp curves are the same as in Fig. 3e, while (cfд) presents results from a numerical simulation using a 0.003 m shift in centre of gravity and a 0.05 kgm² increase in moment of inertia.

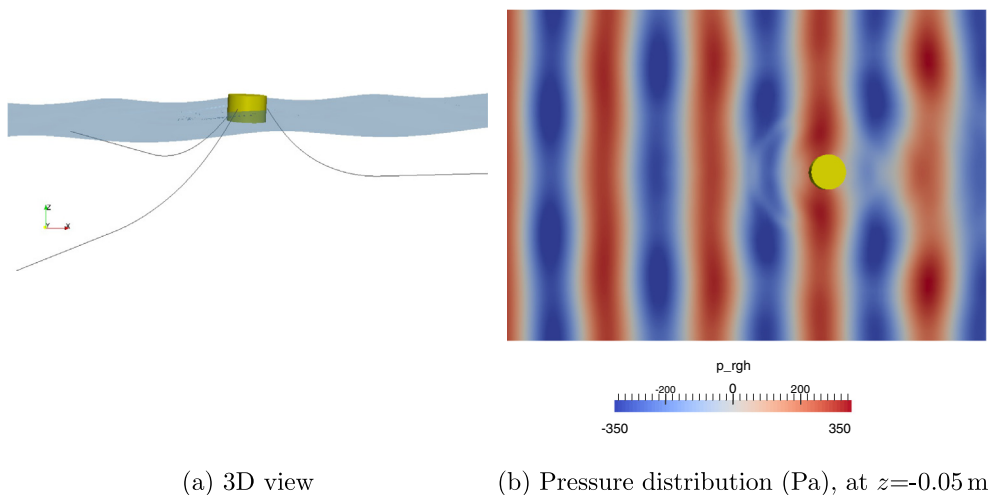


Fig. 5. Snapshot of the solution of the T12H8 case at $t = 39.6$ s.

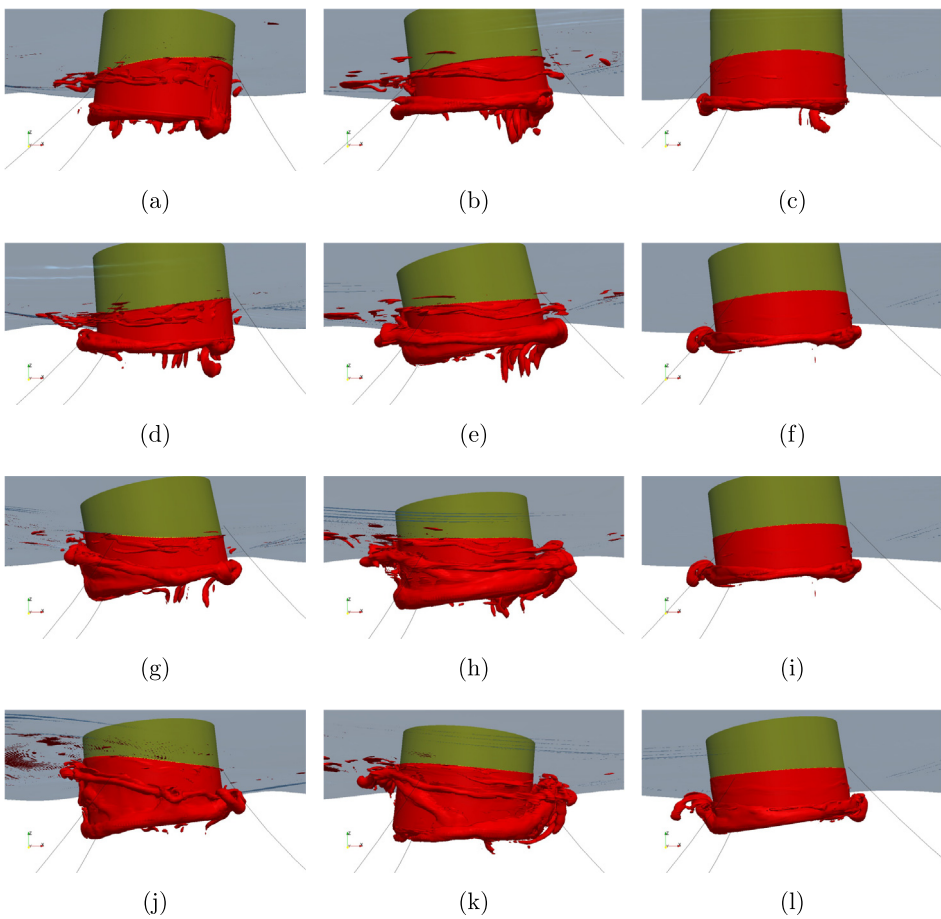


Fig. 6. Typical vortex shedding sequence for the three steep wave cases: T10H8 (left), T12H8 (center) and T14H8 (right). The snapshots are taken every 0.2 s. The figure shows vorticity structures by the $|\nabla \times \mathbf{u}| = 15$ isosurface.

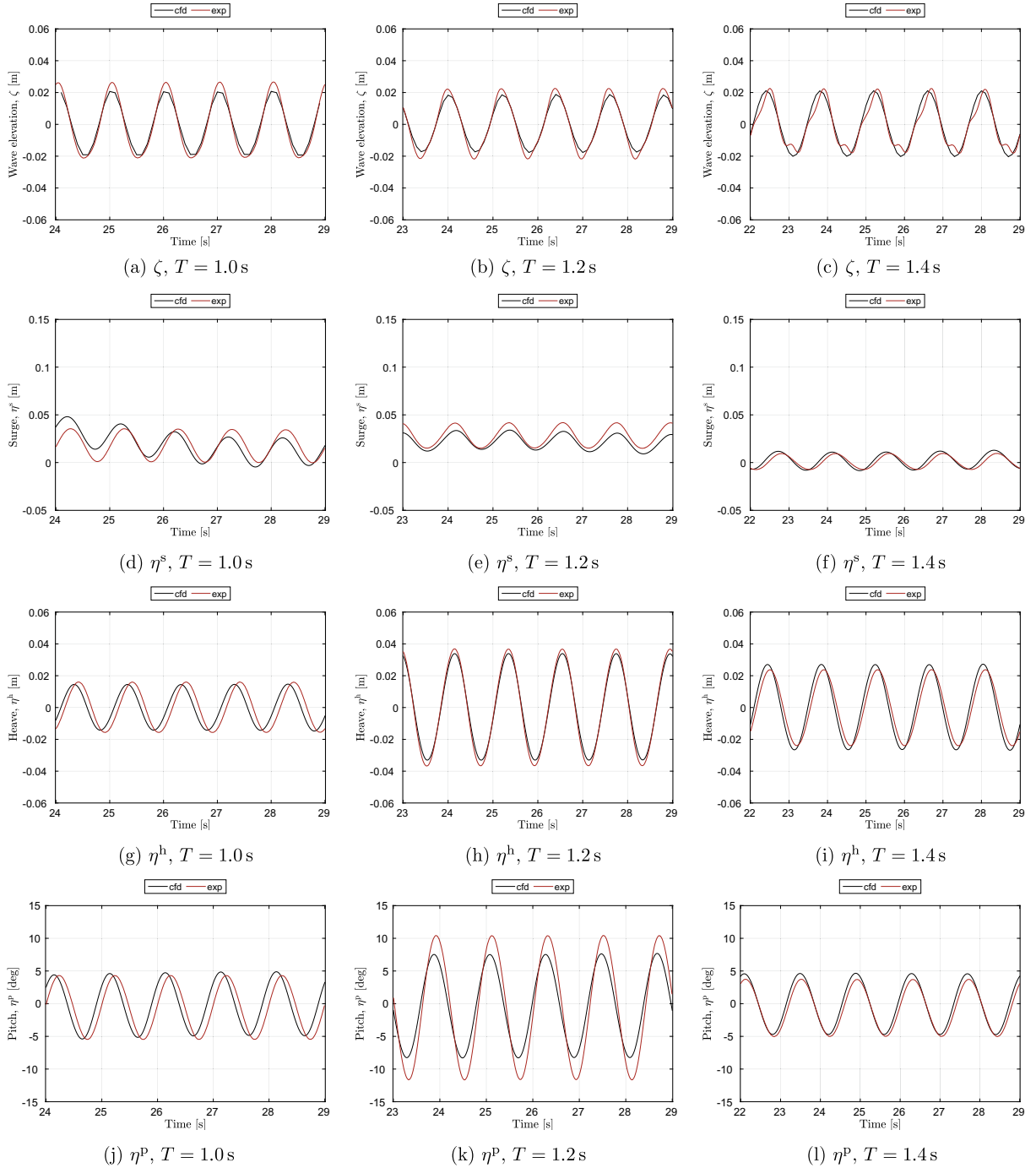


Fig. 7. Sample time history of 5 periods of regular waves with target wave height $H = 0.04\text{ m}$, showing both numerical (cfd) and experimental (exp) values.

7.3.2. Time histories

Time histories of the wave elevation and the body response in surge, heave and pitch over five wave periods are presented in Figs. 7 and 8. Mooring forces from the corresponding cases are shown in Fig. 9. Phase alignment was achieved by shifting the experimental wave amplitude measurements to the phase of the CFD wave, see e.g. Fig. 7a.

The computed and the experimental wave profiles are shown in Figs. 7(a)–(c) and 8(a)–(c). The experimental wave height is in some cases differing from the target wave height. There was no compensation for this in the CFD simulations and the target wave height was used directly as an input to the simulations. The simulated wave profile is computed from the volume fraction iso-surface $\alpha = 0.5$. The measured wave is not only the incoming wave, as also radiated, diffracted and reflected

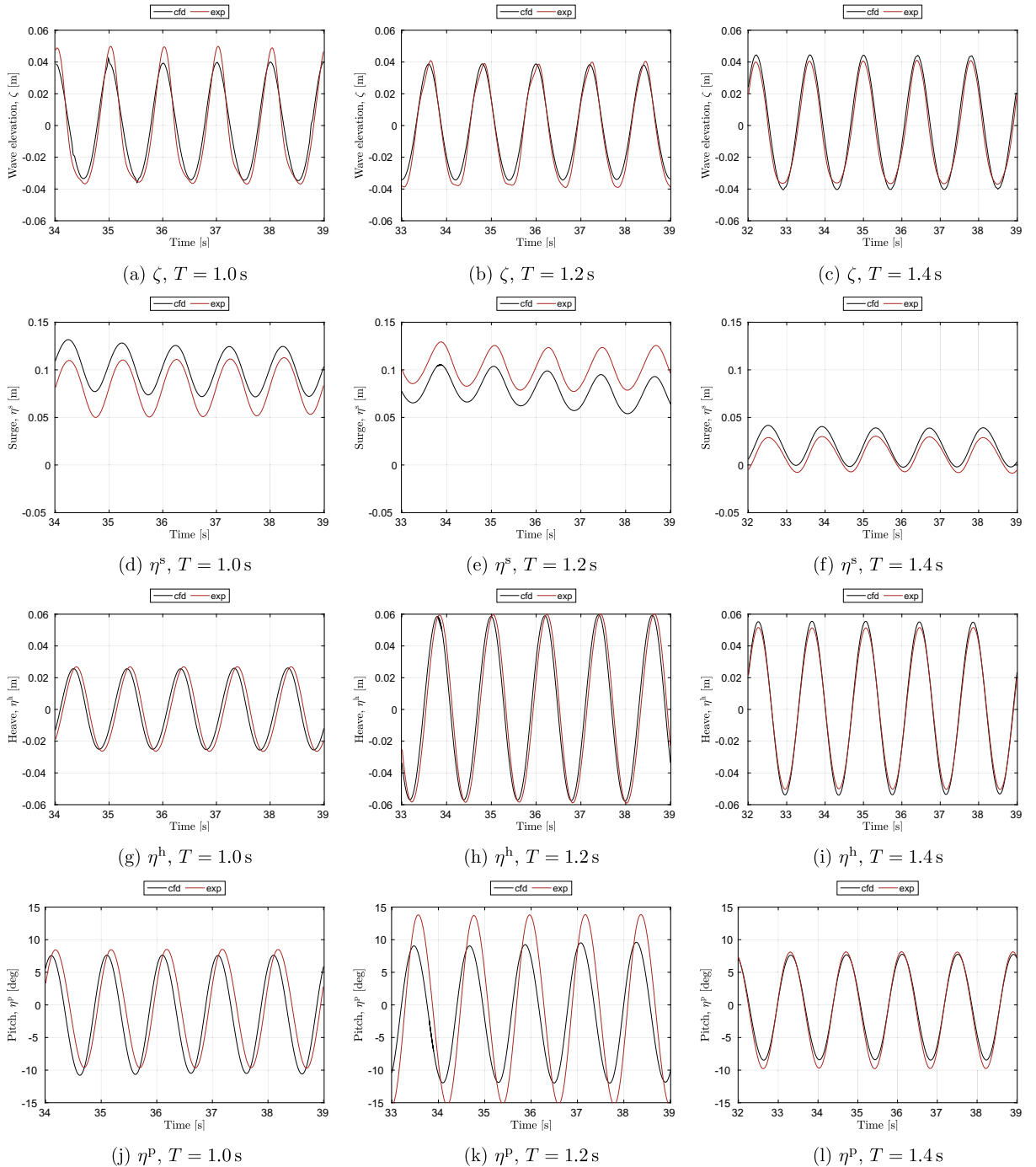


Fig. 8. Sample time history of 5 periods of regular waves with target wave height $H = 0.08\text{ m}$, showing both numerical (cfd) and experimental (exp) values.

waves at the probe location are included. This is clearly seen from the interference pattern in the experimental results of Fig. 7c. As there is no trace of this in the higher wave in Fig. 8c, this is believed to originate from reflections from the basin sides or the absorption beach of the experimental tank. The wave probe is located outside the fine region around the body shown in Fig. 2, where radiated waves are under-resolved to minimise reflections from the side walls.

There is a very good fit between experimental and computed results for heave. The surge response is also generally good, especially in the cases of smaller wave height. However, we see discrepancies in the surge motion for the T10H8 and T12H8 cases, where the mean drift forces are large (see Fig. 8d and e).

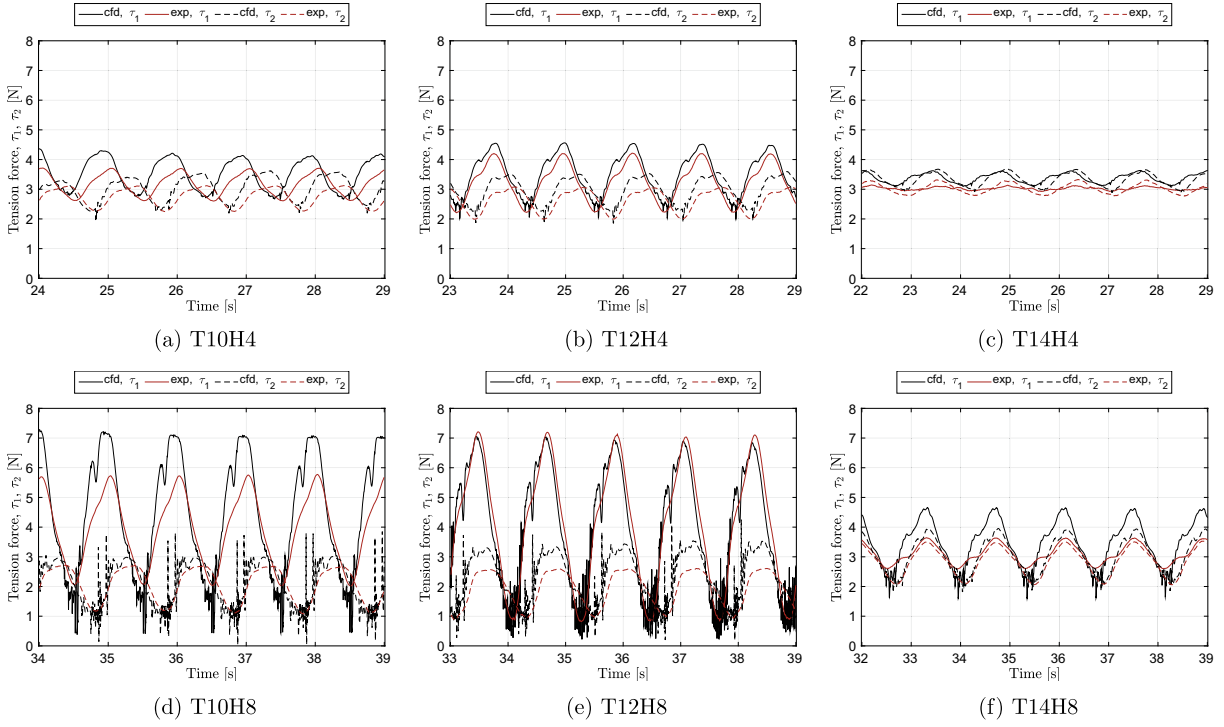


Fig. 9. Time histories of tension force in leg 1 (τ_1) and leg 2 (τ_2). Both experimental values and numerical simulations are presented.

The tension force is on average higher in the CFD simulation than in the experiments. It is also clear that the largest tension comes in the seaward cable in cases of large surge drift offset (compare with e.g. Fig. 8(d)–(f)). For cases of little or no drift, the force amplitudes of the leeward and seaward mooring legs are similar in amplitude. There is a good match between simulations and experiments in terms of the shape of the tension time history. This includes the extra hump seen when the tension is rising up to the crest in e.g. Fig. 9f. For the steeper waves in Fig. 9d and e this hump is however transformed to a clear double peak in the simulations, while remaining a flattened profile in the experimental results.

The over-estimation of the maximum force in the seaward cable seen in the T10H8 case (Fig. 9d) is partly explained by the higher surge offset in the simulations. The leeward cable force is very close to the experimental, but taking the over-predicted surge offset into account the value should be somewhat higher and thus be more in line with the overall trend in the results. In the case of T14H4, the buoy motion is well matched, but the force in the seaward cable is substantially higher than in the corresponding experiment. A possible explanation is that the mooring cable forces are computed under still water conditions, while the experimental cable is affected by the full wave pattern around the buoy.

The numerical noise seen in the region of low tension originates from cable slack in the region around the touch-down point. As MooDy is modelled without bending stiffness, the problem is ill-posed under negative tension [36]. This causes numerical oscillations for short period of time after the tension is recovered.

The pitch response is well captured by the numerical model in the $T = 1.0$ s and $T = 1.4$ s cases, but is under-predicted in the resonance region case with $T = 1.2$ s. This is in line with the results from the decay tests, which showed a faster, and more damped response in the simulations.

8. RAOs

The CFD results for surge, heave and pitch response amplitude operators (RAOs) are in Fig. 10 plotted on top of the experimental RAOs from [24]. There is an excellent match between CFD results and experimental values for surge and heave, but in pitch we see that the CFD simulations under-predicts the resonant response compared with the experiments. Note that the decay test results showed a difference in the natural pitch period of 0.04 s. This corresponds to a slight shift of the expected pitch RAO, which partly explains the discrepancy. The excessive damping seen in the decay tests is also in line with the under-predicted pitch RAO.

The experimental results show a clear wave height dependence of the response amplitude operator (RAO), when comparing responses in $H = 0.04$ m and $H = 0.08$ m regular waves. This non-linearity is well captured by the numerical model, especially for the heave response. This can partly be explained by the mooring force response. The increase in dynamic tension of cable 1 in going from T12H4 to T12H8 first indicates that the lowered RAO peak originates from the increased

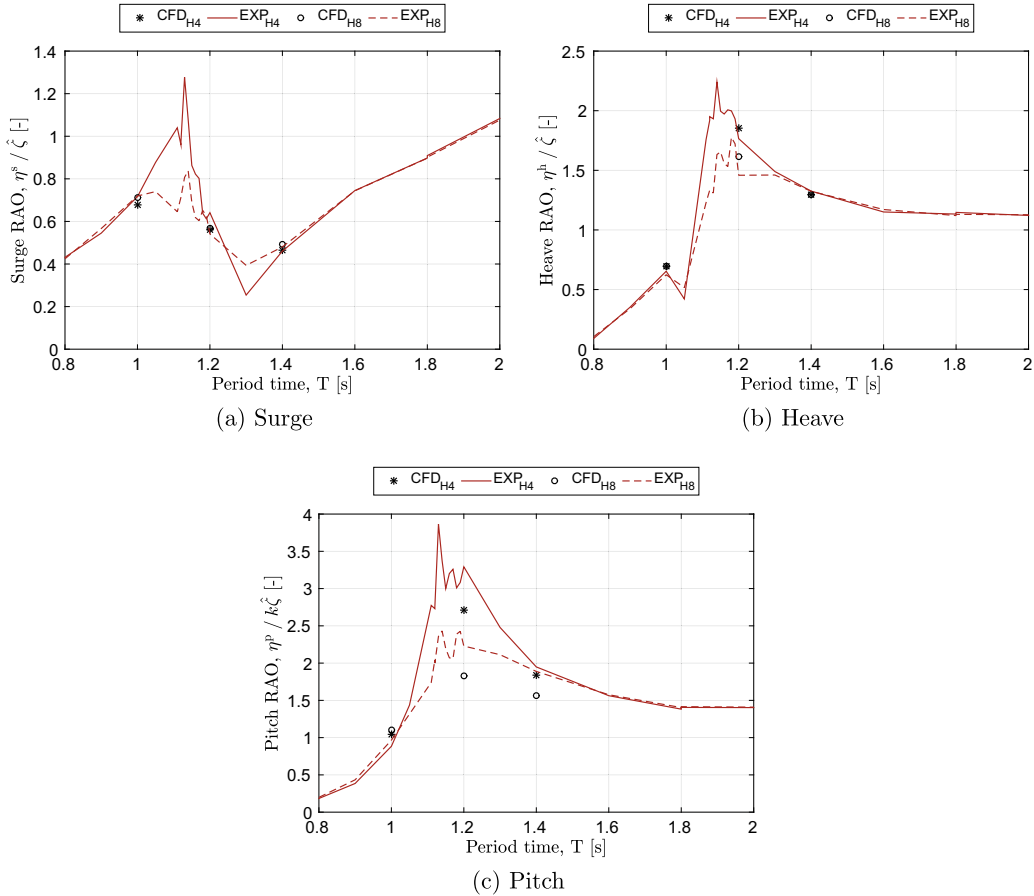


Fig. 10. Response amplitude operators for surge, heave and pitch from experiments [24], compared with CFD results.

mooring stiffness alone, see Fig. 9. However in [24] the same non-linear heave RAO behaviour was seen also for two other mooring configurations (and the same buoy). The increase in dynamic tension was in these cases sub-linear with respect to the wave height, suggesting another driving factor behind the RAO decrease. During large amplitude motion, the instantaneous added mass, radiation damping and draft are all affecting the hydrodynamic forces, with resulting deviations from the approach of linearisation around the mean water level. Also [12] showed the same flattening of the resonance peak for heave of a two body WEC without moorings but with power take off. All in all this consistently implies that the non-linear response is mainly due to the underlying hydrodynamic interaction, but that the effect of the moorings cannot be overlooked.

9. Concluding remarks

We have presented a method for coupled mooring analysis using CFD simulations. The model framework covers most of the important physical effects as it combines the capabilities of VOF-RANS simulations and mooring cable dynamics. The coupling was implemented between the native six DoF motion solver of OpenFOAM and an in-house mooring code, MooDy. It enables detailed studies of the moored motion of floating WECs. Numerical results of a moored floating vertical cylinder in six DoFs are compared with experimental data for validation. Results from decay tests and six cases of regular waves were presented.

There was an excellent match between the experimental and the numerical results for the surge decay test. As the surge response is solely governed by the moorings interacting with the body, the good match gives confidence in the numerical implementation of the coupling.

The overall responses in surge and heave were well captured and there was a fair agreement in mooring force. However, the pitch response was under-predicted in the resonance region. This is partly explained by uncertainties and simplifications in input data of the buoy properties and geometry. There are also modelling uncertainties related to the turbulence model used for modelling the viscous forces.

The coupled model is able to capture the non-linear wave height dependence of the RAOs. We conclude that the non-linear mooring stiffness of the catenary slack mooring configuration does decrease the RAO value for increasing wave heights, but that this cannot be the only explanation. The non-linearity results in a 10–20% decrease of heave RAO in the

$T = 1.2$ s wave, but its significance in irregular waves remains to be determined. As this non-linearity has a strong bearing on the power production [12,5], it is important that it is considered in the design of WECs. This study was made without the presence of a power take off (PTO). Adding a PTO is expected to further increase the drift forces and the viscous impact on the body motion. Further studies investigating the non-linear wave height dependence of the response in irregular waves in operational conditions with PTO are therefore needed to clarify its impact on power production.

CFD simulations of the type presented in this paper are too computationally demanding to be used for long-term estimation of power production. For example [37] reported needing approximately 1000 h on 128 cores for a complete sea-state of a full scale Wave Dragon device. The regular waves presented in this study were computed on 128 cores (65,000 cells/core) with a computation time in the order of 10 h per period for the higher waves. CFD methods are thus not to be seen as a replacement for faster methods such as radiation-diffraction codes, but rather as a valuable bridge between simplified approaches and costly experimental investigations [11]. The results presented in this paper give confidence in the model capability to capture non-linear effects in the resonance region. The completeness of the method makes it a suitable candidate to study the individual influence of different non-linearities acting on WECs, as contributions from different physical effects can be analysed independently in the same framework. Future studies will focus on scale effects and viscosity influence on floating WECs under operational and survival conditions.

Acknowledgements

Support for this work was given by the Swedish Energy Agency under grant no. P40428-1. The simulations were made on resources from Chalmers Centre for Computational Science and Engineering provided by the Swedish National Infrastructure for Computing. We also acknowledge the support from the Portuguese Foundation for Science and Technology through the research grant SFRH/BD/62040/2009 and the POPH/FSE program.

References

- [1] Ocean energy: State of the art [online], Tech. rep., SI Ocean, available: <http://si-ocean.eu> (December 2012).
- [2] J. Weber, R. Costello, J. Ringwood, Wec technology readiness and performance matrix – finding the best research technology development trajectory, in: Proc. ICOE 2012, Dublin, Ireland, 2012.
- [3] L. Johanning, G. Smith, J. Wolfram, Measurements of static and dynamic mooring line damping and their importance for floating WEC devices, *Ocean Eng.* 34 (2007) 1918–1934.
- [4] M. Retes, A. Merigaud, J. Gilloteaux, J. Ringwood, Nonlinear Froude–Krylov force modelling for two heaving wave energy point absorbers, in: Proc. EWTEC 2015, Nantes, France, 2015.
- [5] M. Bhinder, A. Babarit, L. Gentaz, P. Ferrant, Potential time domain model with viscous correction and CFD analysis of a generic surging floating wave energy converter, *Int. J. Marine Energy* 10 (2015) 70–96.
- [6] A. Nematabakhsh, C. Michailides, Z. Gao, T. Moen, Comparison of experimental data of a moored multibody wave energy device with a hybrid CFD and BIEM numerical analysis framework, in: Proc. OMAE 2015, St John's, Canada, 2015.
- [7] L. Larsson, F. Stern, M. Visonneau, *Numerical Ship Hydrodynamics*, Springer, New York, 2010.
- [8] N. Jacobsen, M. van Gent, G. Wolters, Numerical analysis of the interaction of irregular waves with two dimensional permeable coastal structures, *Coastal Eng.* 102 (2015) 13–29.
- [9] Y. Li, M. Lin, Regular and irregular wave impacts on floating body, *Ocean Eng.* 42 (2012) 93–101.
- [10] P. Higuera, J. Lara, I. Losada, Realistic wave generation and active wave absorption for Navier–Stokes models application to OpenFOAM, *Coastal Eng.* 71 (2013) 102–118.
- [11] J. Kim, R. Izarra, H. Jang, J. Kyong, J. O'Sullivan, An application of the eom-based numerical basin to dry-tree semisubmersible design, in: Proc. Offshore Symposium 2014, Houston, USA, 2014.
- [12] Y. Yu, Y. Li, Reynolds-averaged Navier–Stokes simulation of the heave performance of a two-body floating-point absorber wave energy system, *Comput. Fluids* 73 (2013) 104–114.
- [13] C. Eskilsson, J. Palm, A. Ensig-Karup, U. Bosi, M. Ricchiuto, Wave induced motions of point-absorbers: an hierarchical investigation of hydrodynamic models, in: Proc. EWTEC 2015, Nantes, France, 2015.
- [14] M. Verdúzco-Zapata, F. Ocampo-Torres, Study of a 6 DOF wave energy converter interacting with regular waves using 3D CFD, in: Proc. 11th EWTEC 2015, 2015.
- [15] Y. Yu, Y. Li, Preliminary results of a RANS simulation for a floating point absorber wave energy system under extreme wave conditions, in: Proc. OMAE 2011, 2011.
- [16] R. Nicholls-Lee, A. Walker, S. Hindley, R. Argall, Coupled multi-phase CFD and transient mooring analysis of the floating wave energy converter OWEL, in: Proc. OMAE 2013, Nantes, France, 2013.
- [17] J. Palm, C. Eskilsson, G. Paredes, L. Bergdahl, CFD simulations of a moored floating wave energy converter, in: Proc. EWTEC 2013, 2013.
- [18] H. Wolgamot, C. Fitzgerald, Nonlinear hydrodynamic and real fluid effects on wave energy converters, in: Proc IMechE Part A: J Power and Energy, 2015.
- [19] OpenCFD Ltd, OpenFOAM homepage. [Online], available <http://www.openfoam.org>, 2014.
- [20] J. Davidson, M. Cathelain, L. Guillemet, T. Le Huec, J. Ringwood, Implementation of an OpenFOAM numerical wave tank for wave energy experiments, in: Proc. EWTEC 2015, Nantes, France, 2015.
- [21] J. Palm, C. Paredes, C. Eskilsson, F. Taveira-Pinto, L. Bergdahl, Simulation of mooring cable dynamics using a discontinuous Galerkin method, in: Proc. MARINE2013, Hamburg, 2013.
- [22] G. Paredes, C. Eskilsson, J. Palm, L. Bergdahl, L. Leite, F. Pinto, Experimental and numerical modeling of a moored, generic wave energy converter, in: Proc. EWTEC 2013, 2013.
- [23] L. Bergdahl, J. Palm, C. Eskilsson, J. Lindahl, Dynamically scaled model experiment of a mooring cable, *J. Marine Sci. Technol.* 4 (2016) 5.
- [24] G. Paredes, J. Palm, C. Eskilsson, L. Bergdahl, F. Taveira-Pinto, Experimental investigation of mooring configurations for wave energy converters, in: Proc. EWTEC 2015, 2015.
- [25] H. Weller, G. Tabor, H. Jasak, C. Fureby, A tensorial approach to CFD using object oriented techniques, *Comp. Phys.* 12 (1998) 620–631.
- [26] N. Jacobsen, D. Fuhrman, J. Fredsoe, A wave generation toolbox for the open-source CFD-library OpenFOAM, *Int. J. Num. Methods Fluids* 70 (2012) 1073–1088.
- [27] A. Ruju, J. Lara, I. Losada, Radiation stress and low frequency energy balance within the surf zone: A numerical approach, *Coastal Eng.* 68 (2012) 44–55.
- [28] T.-H. Shih, J. Zhu, J.L. Lumley, Calculation of wall-bounded complex flows and free shear flows, *Int. J. Num. Methods Fluids* 23 (1996) 1133–1144.

- [29] Orcina Inc, OrcaFlex manual – version 9.5a, 2012.
- [30] J. Lindahl, Implicit numerisk lösning av rörelsekvationerna för en förankringskabel, in: Tech. Rep. Report Series A:11, Chalmers University of Technology, 1984.
- [31] B. Cockburn, C.-W. Shu, Runge–Kutta discontinuous Galerkin methods for convection-dominated problems, *J. Sci. Comp.* 16 (2001) 173–261.
- [32] J. Palm, Developing computational methods for moored floating wave energy devices, Lic. Eng. Thesis. Report No. 14:151, 2014.
- [33] R. Dean, R. Dalrymple, *Water Wave Mechanics for Engineers and Scientists*, World Scientific, 1991.
- [34] T. Sarpkaya, M. Isaacson, *Mechanics of Wave Forces on Offshore Structures*, Van Nordstrand Reinhold, New York, 1981.
- [35] P. Lin, P. Liu, A numerical study of breaking waves in the surf zone, *J. Fluid Mech.* 359 (1998) 239–264.
- [36] M. Triantafyllou, C. Howell, Dynamic response of cables under negative tension: An ill-posed problem, *J. Sound Vib.* 173 (4) (1994) 433–447.
- [37] C. Eskilsson, J. Palm, J. Kofoed, E. Friis-Madsen, CFD study of the overtopping discharge rate of the Wave Dragon wave energy converter, in: C. Guedes Soares (Ed.), *Renewable Energies Offshore*, Taylor & Francis Group, 2014, pp. 287–294.